nature energy

Article

https://doi.org/10.1038/s41560-022-01177-5

# Imaging of nitrogen fixation at lithium solid electrolyte interphases via cryo-electron microscopy

Received: 8 April 2022

Accepted: 11 November 2022

Published online: 22 December 2022

Check for updates

Katherine Steinberg [1,5], Xintong Yuan [2,5], Channing K. Klein [3], Nikifar Lazouski[1], Matthew Mecklenburg[4], Karthish Manthiram [3] ✉ & Yuzhang Li [2] ✉

Ammonia is an important industrial chemical and is also being discussed as a potential energy carrier. Electrifying ammonia synthesis could help to decarbonize the chemical industry, as the Haber–Bosch process contributes markedly to global carbon emissions. A lithium-mediated pathway is among the most promising ambient-condition electrochemical ammonia synthesis methods. However, the role of metallic lithium and its passivation layer, the solid electrolyte interphase (SEI), remains unresolved. Here we use cryogenic transmission electron microscopy as part of a multiscale approach to explore lithium reactivity and the SEI, discovering that the proton donor (for example, ethanol) governs lithium reactivity towards nitrogen fixation. Without ethanol, the SEI passivates lithium metal, rendering it inactive for nitrogen reduction. Ethanol disrupts this passivation layer, enabling continuous reactivity at the lithium surface. As a result, metallic lithium is consumed via reactions with nitrogen, proton donor and other electrolyte components. This reactivity across the SEI is vital to device-level performance of lithium-mediated ammonia synthesis.

With an annual production of over 175 million tons (ref. [1]), ammonia ($NH_3$) is among the most important commodity chemicals. While ~80% of ammonia is used in producing fertilizers[2,3], it is also the main source of nitrogen functionality in chemical synthesis[4] and may be a key energy carrier as industry decarbonizes[1,5]. The predominant method of ammonia generation is the Haber–Bosch process, which demands high temperatures (400–500 °C) and pressures (150–250 bar) to react nitrogen and hydrogen, usually using hydrogen from steam-methane reforming[5,6]. As a result, each ton of ammonia produced generates upwards of 1.9 tons of $CO_2$, contributing 1–2% of global carbon emissions[7,8]. Due to the complexity of the Haber–Bosch process, it is only economical at large scales, leading to centralized production that creates disparities in access to fertilizer[7,9]. These limitations motivate the development of electrochemical ammonia synthesis methods, which could be modular, easily integrated with intermittent renewable electricity, and use water electrolysis, eliminating the need for hydrocarbon-derived hydrogen[8,10].

One of the most promising ambient-condition electrochemical methods for ammonia synthesis is the lithium-mediated pathway. This process takes advantage of the facile and thermodynamically favourable reaction between dinitrogen and metallic lithium (Supplementary Note 5)[11], generating ammonia by electrodepositing lithium from an organic electrolyte, often $LiBF_4$ or $LiClO_4$ in tetrahydrofuran (THF) that contains nitrogen and a proton donor[12–15]. Lithium-mediated electrochemical ammonia synthesis (LiMEAS) has been rigorously vetted by control experiments[14–16] and achieves the highest rates and

[1]Department of Chemical Engineering, Massachusetts Institute of Technology, Cambridge, MA, USA. [2]Department of Chemical & Biomolecular Engineering, University of California, Los Angeles, Los Angeles, CA, USA. [3]Division of Chemistry and Chemical Engineering, California Institute of Technology, Pasadena, CA, USA. [4]California NanoSystems Institute (CNSI), University of California, Los Angeles, Los Angeles, CA, USA. [5]These authors contributed equally: Katherine Steinberg and Xintong Yuan. ✉e-mail: karthish@caltech.edu; yuzhangli@ucla.edu

https://doi.org/10.1038/s41560-022-01177-5

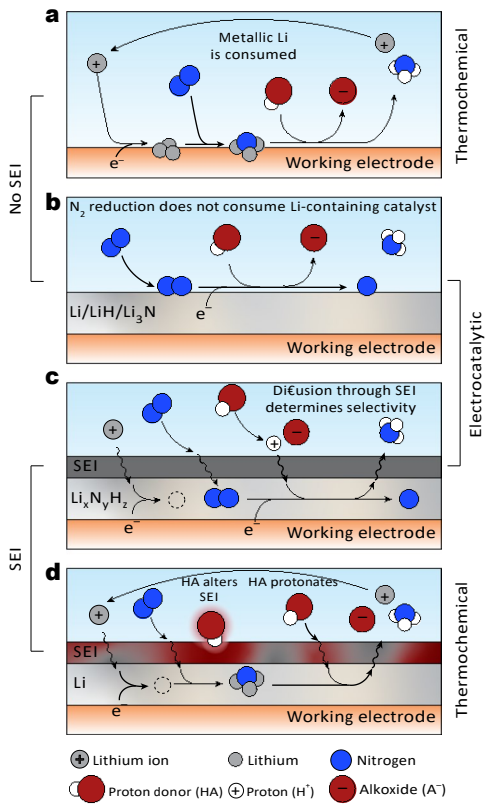


**Fig. 1 | Previously proposed reaction mechanisms of lithium-mediated ammonia synthesis. a**, Thermochemical mechanism proposed in ref. [14]. **b**, Electrocatalytic mechanism proposed in ref. [23]. **c**, SEI transport model proposed in ref. [21]. **d**, SEI permeability model proposed in ref. [29].

Faradaic efficiencies (FEs) to date among ambient-temperature electrochemical ammonia synthesis processes[17–19]. The efficiency of LiMEAS has improved appreciably from its first reported implementations in 1930[20] and 1993[12] with developments such as the use of gas diffusion electrodes[17], pulsed currents[21], a phosphonium salt proton shuttle[18] and the addition of low concentrations of oxygen[19].

However, the role of lithium in LiMEAS is still under debate. Some studies propose that electrochemically deposited lithium is consumed by thermochemical nitridation and protonation steps to generate ammonia and lithium ethoxide—a pathway classified as thermochemical because the nitrogen fixation step is thermochemical (Fig. 1a)[12–14,22]. Other works propose an electrocatalytic mechanism in which a layer of lithium, lithium nitride or lithium hydride adsorbs, protonates and reduces nitrogen to make ammonia without being consumed, thereby acting as an electrocatalyst (Fig. 1b)[21,23].

A potential source of complexity in LiMEAS is the possible formation of a passivation film called the solid electrolyte interphase (SEI). The SEI forms spontaneously in all electrochemical lithium cells because the Fermi level of metallic lithium is higher than the lowest unoccupied molecular orbital of practical electrolytes, causing electrolyte reduction at the lithium-metal surface[24,25]. The SEI can vary in composition and structure depending on electrolyte chemistry and operating conditions, though it is usually electronically insulating and ionically conductive[26,27]. Its local properties dictate transport of lithium ions at the electrode–electrolyte interface and thus the morphology of lithium deposits[28].

The SEI is often invoked to explain observed phenomena in LiMEAS, yet our understanding of its role is still incomplete. One study proposes that relative transport rates of lithium ions, nitrogen and protons through a non-reactive SEI are the most influential factor in determining selectivity, with imbalance in diffusion rates leading to undesirable build-up of metallic lithium or lithium nitride or excessive hydrogen evolution (Fig. 1c)[21]. Our group has also emphasized the importance of transport through the SEI, proposing that proton donor identity and concentration impact whether the SEI is permeable to nitrogen diffusion (Fig. 1d)[29]. Other works have taken steps to directly detect surface species in LiMEAS, using lithium stripping[22,23,30], titration measurements of lithium nitride[14,23,30] and X-ray characterization techniques[19,30] to probe surface chemistry. While these studies provide insights into the composition of the lithium surface, none yet have resolved the debate over the molecular-scale mechanism of LiMEAS because lithium metal and its SEI cannot be characterized with sufficient spatial resolution using conventional techniques.

Here we have taken a multiscale approach to understanding of the role of surface chemistry in LiMEAS. We combined bulk quantification of key products, scanning electron microscopy (SEM), and X-ray photoelectron spectroscopy (XPS) with cryogenic electron microscopy (cryo-EM), leveraging the nanoscopic resolution that has given this technique such utility in the battery field[27,28,31,32]. We observed that lithium nitridation is highly sensitive to surface passivation; in the absence of a proton donor (for example, ethanol), the SEI inhibits reactivity between lithium and nitrogen. We found that the addition of ethanol disrupts the formation of a passivating SEI, enabling continuous surface reactivity that consumes metallic lithium as it deposits. The data indicate that LiMEAS operates via continuous thermochemical consumption of poorly passivated lithium, making it a rare application of lithium electrochemistry that requires corrosion-type reactions to occur across the SEI.

## Model systems for systematic study of surface reactivity

Most of what is known about the SEI is from research on lithium batteries, which generally use aprotic organic solvents and inert argon atmospheres. In contrast, LiMEAS has two added sources of reactivity: a proton donor and nitrogen gas. We set out to understand how these components change the surface chemistry of lithium by varying the presence of each species in four model systems: system A with Ar gas, no proton donor ('no HA, Ar'); system B with $N_2$ gas, no proton donor ('no HA, $N_2$'); system C with Ar gas, 0.1 M EtOH ('EtOH, Ar'); and system D with $N_2$ gas, 0.1 M EtOH ('EtOH, $N_2$').

It is important to note that the conditions used—ambient pressure, ethanol as proton donor, low current density and flooded electrodes—were chosen for ease of characterization, not for optimal performance (Fig. 2a and Supplementary Note 2).

## Quantification of key products

To better understand reactivity at the lithium surface in LiMEAS, the major reaction products were quantified for each of the four model systems, revealing that the presence or absence of proton donor is the most important factor in determining the partitioning of FE.

Ammonia can be measured using the salicylate assay[14,33], while lithium nitride or other fixed nitrogen species ($Li_xN_yH_z$) can be quantified via acid titration followed by the salicylate assay, keeping in mind potential limitations with detecting small amounts of ammonia (Supplementary Methods). Unsurprisingly, only system D, which contains both nitrogen and ethanol, generates appreciable ammonia at FEs averaging 5.8% (Fig. 2c). On the basis of most proposed mechanisms (Fig. 1a–c) and the thermodynamic favourability of lithium nitride formation (Supplementary Note 5), we might expect that the lithium nitride FE for cells with nitrogen feed gas and no proton donor (system B) would be close to 5.8%. However, we find that while lithium nitride yields are reliably between 0.2% and 0.4% FE in the presence of both nitrogen and ethanol, they are much more variable, and on average lower, in the absence of proton donor (Fig. 2d and Supplementary Fig. 4).

https://doi.org/10.1038/s41560-022-01177-5

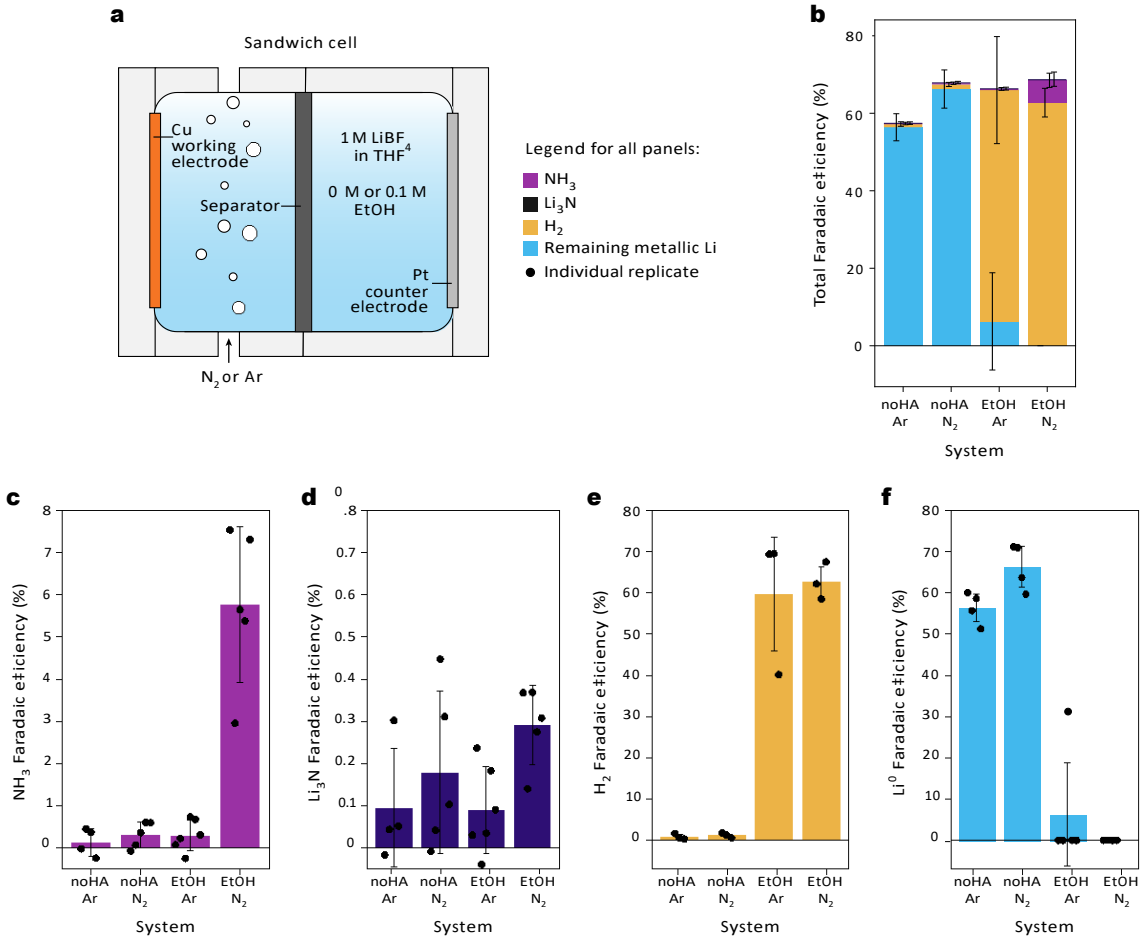


**Fig. 2 | Quantification of key products. a**, Diagram of cell set-up used in these experiments. All experiments used a current density of −3 mA cm$^{-2}$, total charge of 1 mAh, ethanol concentration of 0 M or 0.1 M and gas flow rate of 10 sccm. Note that the legend included in **a** applies to all panels. **b**, Total Faradaic efficiencies of quantified products, stacked vertically for each model system in the order $Li^0$, $H_2$, $NH_3$ and $Li_3N$, from bottom to top. Bars represent the mean of replicates shown in **c**–**f**, with error bars showing one standard deviation. Error bars are staggered such that they represent $Li^0$, $H_2$, $NH_3$ and $Li_3N$ from left to right and are centred vertically at the top of the bar for each species. **c**, Average ammonia Faradaic efficiencies, $n = 4, 5, 6, 5$ for the model systems from left to right. **d**, Average lithium nitride Faradaic efficiencies, $n = 4, 5, 6, 5$ for model systems from left to right. **e**, Average dihydrogen Faradaic efficiencies, $n = 3$ for all model systems. **f**, Average electrochemically connected remaining metallic lithium Faradaic efficiencies, $n = 4$ for all model systems except 'EtOH, Ar,' for which $n = 5$. For all plots, black circles mark the FE of individual experimental replicates, bars mark the mean of all replicates and error bars are one standard deviation. Raw data are included in source data.

A 24-hour electrochemical experiment and an analogous experiment using lithium foil dipped in electrolyte also fail to generate lithium nitride in the absence of proton donor (Supplementary Figs. 5 and 6). These data suggest that the reaction between lithium and nitrogen is suppressed in the absence of proton donor, perhaps because dinitrogen cannot easily permeate the native SEI film formed via reduction of electrolyte on lithium without ethanol present. In agreement with previous measurements[14,23,30], the detected $Li_3N$ in system D occurs in very small quantities, supporting the hypothesis that the protonation step in LiMEAS is fast, and fixed nitrogen species are short-lived on the electrode surface[14,30].

Another important side product in LiMEAS is hydrogen gas, which can be quantified via online gas chromatography (GC) measurements (Fig. 2e). The hydrogen FE increases from <2% in the absence of proton donor to ~60% with the addition of ethanol, indicating that the majority of generated hydrogen originates from ethanol. Because only 1 mAh of charge is passed in total, the $H_2$ FEs with proton donor reflect only ~6–7% consumption of the ethanol in the electrolyte (Supplementary Fig. 7a). The average $H_2$ FE with proton donor appears independent of feed gas, though the argon case has greater variability. Hydrogen measured in the absence of proton donor is probably the result of trace water reduction or possibly the reduction of THF or oxidized THF products that diffuse from the counter electrode (Supplementary Note 6).

By galvanostatically stripping the electrode after experiments, we can obtain an estimate of the electrochemically connected metallic lithium remaining on the surface (Fig. 2f)[34,35]. Once again, the strongest predictor of yield in this measurement is the presence or absence of proton donor, with the systems lacking proton donor accumulating strippable lithium corresponding to more than half the charge passed. In the cases with ethanol added, all but one of the replicates we performed had zero electrochemically connected lithium (Supplementary Figs. 9 and 10). This result differs from previous findings in the literature[23,30] and appears to depend heavily on electrolyte composition (Supplementary Figs. 12 and 32e and Supplementary Note 4). Overall, it appears that when ethanol is present in *this* electrolyte, metallic lithium is largely consumed through reactions with ethanol, nitrogen and other electrolyte components.

Summing the FEs of quantified products accounts for 60–70% of the total charge passed (Fig. 2b). This is reasonable for lithium electroplating, as the remaining charge probably goes to 'inactive' or non-electrochemically connected lithium and the formation of SEI (Supplementary Note 7)[35].

https://doi.org/10.1038/s41560-022-01177-5

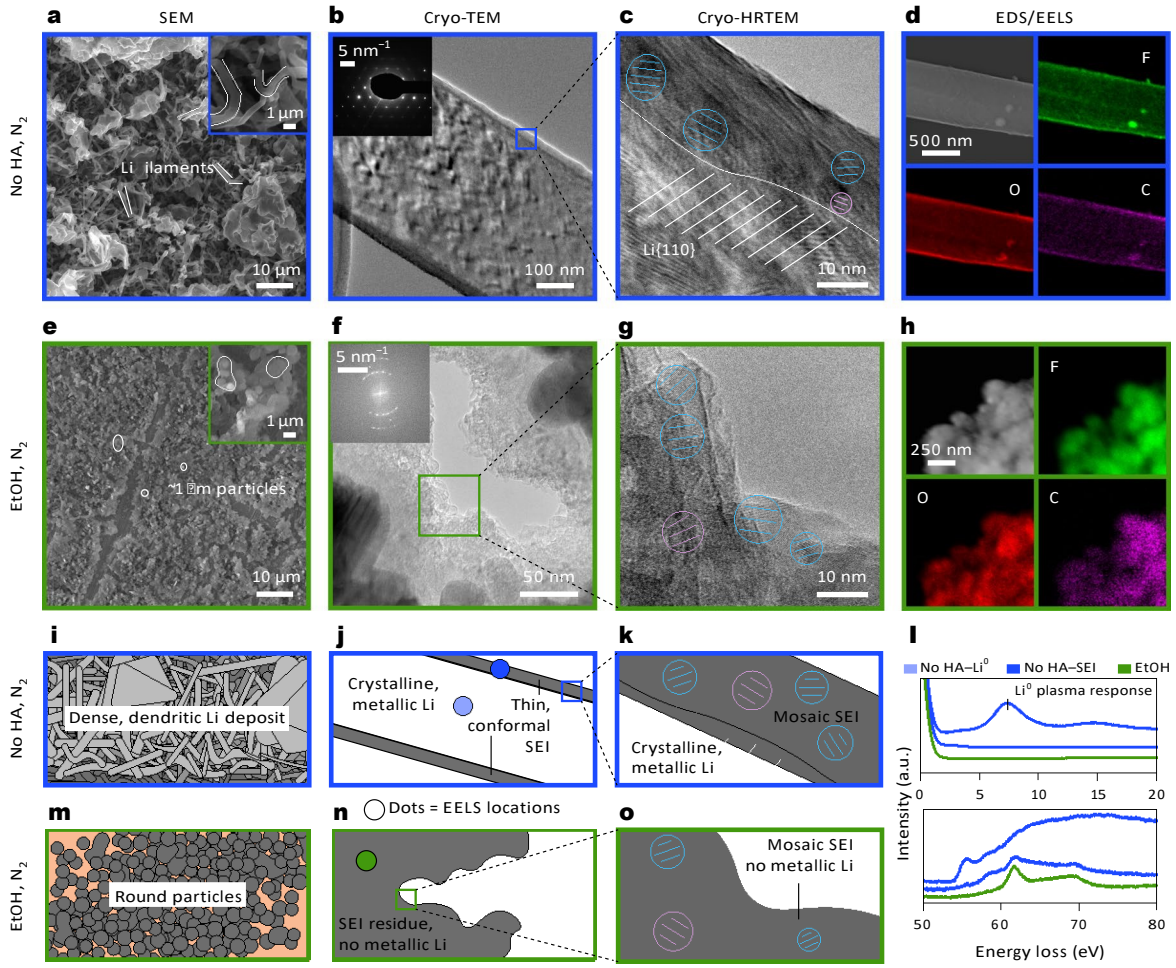


**Fig. 3 | Imaging results from the 'no HA, $N_2$' and 'EtOH, $N_2$' model systems.** **a**, SEM image of the 'no HA, $N_2$' system, with inset at higher magnification. **b**, Cryo-TEM image of the 'no HA, $N_2$' system, with inset SAED image. **c**, High-resolution cryo-TEM image of the 'no HA, $N_2$' system, with the Li lattice and several of the mosaic SEI crystalline regions annotated. **d**, Cryo-STEM EDS mapping of the 'no HA, $N_2$' system. **e**–**h**, analogous images to **a**–**d** but collected on the 'EtOH, $N_2$' system. Note that **f** includes an inset fast Fourier transform of image **g** rather than SAED, but both are included in Supplementary Fig. 24. **i**–**k**,**m**–**o**, Illustrations of the morphology observed at different scales of imaging for each sample. Dots in **j** and **n** represent the three regions used to generate EELS spectra in **l**. **l**, Representative cryo-STEM EELS spectra of the 'no HA, $N_2$' sample collected in the metallic Li region (light blue) and the SEI region (darker blue) and of the 'EtOH, $N_2$' sample. Top plot displays the low-loss region, and bottom plot displays the Li K-edge core-loss region. Enlarged versions of all the images shown here and corresponding images for Ar-feed gas model systems can be found in Supplementary Figs. 13–26.

## Imaging the lithium surface

Our product quantification results indicate stark differences in reactivity with and without proton donor, even for reactions that do not directly involve ethanol. To understand this phenomenon, we reveal surface morphology using SEM. Figure 3 includes imaging data from the model systems with $N_2$ both with and without ethanol, and complete results for all four model systems can be found in Supplementary Figs. 13–26. For the two cases without proton donor, the lithium deposits are essentially identical in morphology, with a mix of lithium filaments and larger agglomerations commonly observed in lithium-metal batteries (Fig. 3a and Supplementary Figs. 14 and 15)[28,31]. With the addition of proton donor, the morphology changes substantially; instead of a dense layer of lithium filaments, there are round deposits that leave the underlying Cu foils exposed in several places (Fig. 3e and Supplementary Figs. 16 and 17). The lower contrast and smearing of the SEM images due to electron beam-induced charging[36] indicates that these particles are electrically insulating, suggesting a strong presence of SEI rather than metallic lithium.

The absence of metallic lithium deposits in systems with ethanol imply that there could be differences in surface passivation with the addition of proton donor. Cryo-EM can preserve these reactive surface structures, allowing us to understand the role of SEI in promoting these morphologies. Metallic lithium and its SEI are highly beam sensitive in conventional transmission electron microscopy (TEM), but cryogenic temperatures stabilize and preserve their native state, enabling high-resolution observation of the SEI[31]. To leverage cryo-EM, we placed TEM grids at the working electrode of each cell, then after the experiment, the grids were plunge frozen in liquid nitrogen (Supplementary Fig. 19). Consistent with previous literature, we saw no evidence of reactivity between metallic lithium and liquid nitrogen in energy-dispersive X-ray spectroscopy (EDS) mapping of cryo-EM samples (Supplementary Fig. 25)[31].

Cryo-TEM reveals that the interfacial morphology of samples without proton donor (systems A and B) resembles other lithium deposits documented in the cryo-EM battery literature[28,31]. Selected area electron diffraction (SAED) patterns reveal crystalline lithium viewed along the [011] and [111] zone axes respectively (Supplementary Fig. 24a, b),

https://doi.org/10.1038/s41560-022-01177-5

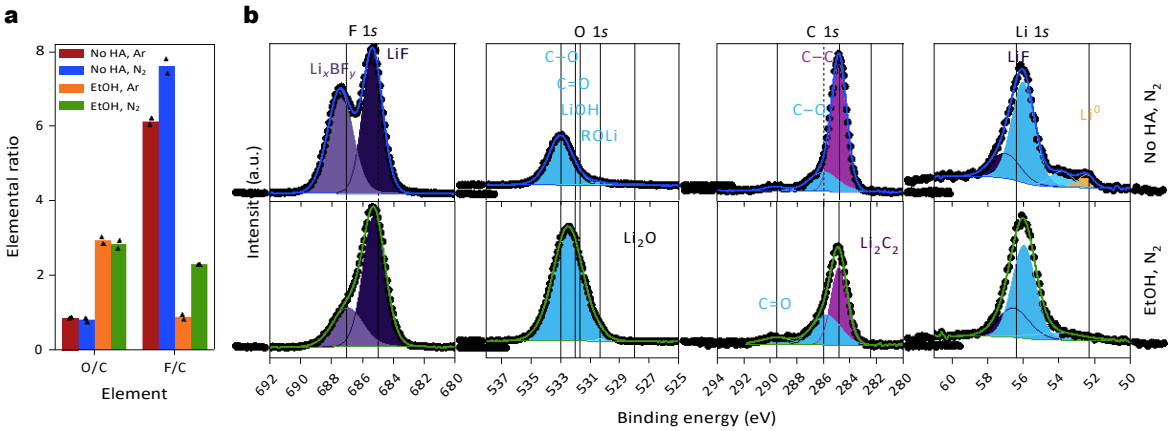


**Fig. 4 | XPS results from the four model systems. a**, Key elemental ratios observed in survey spectra of each system. Black triangles mark the elemental ratios in two different locations on each sample, and coloured bars mark the mean elemental ratio of the two locations. **b**, High-resolution spectra for 'no HA, $N_2$' and 'EtOH, $N_2$' systems. The intensity scale on the *y* axis is consistent for plots of the same element. Vertical dashed lines mark known binding energies of relevant species. More spectra can be found in Supplementary Figs. 27 and 28. Methods provide details about fitting.

and in high-resolution images, it is possible to measure lattice spacings consistent with the {1$\bar{1}$0} planes of crystalline Li (Fig. 3c and Supplementary Figs. 20 and 21). The SEI is observed as a darker-contrast region at the surface of the Li filaments, approximately 20–30 nm in thickness. It appears to have a mosaic structure, with nanoscale regimes of crystalline, inorganic materials interspersed among organic, amorphous species (Fig. 3c)[31]. On the basis of measurements of the lattice spacings, these inorganic regions appear consist of LiF and LiOH or $Li_2O$, with XPS results supporting the presence of LiF and LiOH (*vide infra*).

With ethanol present in the electrolyte, the clean metallic lithium–SEI interface disappears, and instead, we observe only SEI-type materials (Fig. 3e and Supplementary Figs. 22 and 23). SAED and fast Fourier transform processing of high-resolution TEM (HRTEM) images show rings characteristic of polycrystalline materials, with lattice spacings consistent with LiF and LiOH (Supplementary Fig. 24c–f). HRTEM reveals a mosaic structure similar to that of the SEI in the 'no HA' cases, with a mixture of crystalline and amorphous regions (Fig. 3g). Lattice spacings in the crystalline regions imply that these consist of LiF and LiOH. The amorphous parts of the deposit are beam sensitive, changing with prolonged imaging.

In addition to imaging and diffraction, cryo-scanning transmission electron microscopy (STEM) EDS mapping was also conducted on all samples. EDS can detect elements heavier than boron, and for each sample, we detect fluorine, oxygen and carbon, but not nitrogen. For 'no HA' samples, these elements are concentrated in the SEI regions and do not appear to vary spatially throughout the SEI, supporting the observation that the SEI is mosaic rather than multilayered in structure (Fig. 3d). Similarly, for 'EtOH' samples, F, O and C appear evenly distributed through the sample (Fig. 3h).

To directly probe the bonding environment of structures observed using cryo-EM, we also conducted cryo-STEM electron energy loss spectroscopy (EELS) on both the 'no HA' and 'EtOH' samples formed with nitrogen feed gas (Fig. 3l and Supplementary Fig. 26). The composition of 'EtOH' samples does not vary much with location, while the 'no HA' samples show clear differences in composition between the regions of crystalline, metallic lithium at the centre of filaments and the SEI coating those areas. Low-loss spectra show that the regions we had identified as crystalline lithium in the 'no HA' sample do indeed exhibit the characteristic plasma response of lithium metal near 7.5 eV (ref. [27]). Li K-edge core-loss spectra further confirm that these regions are metallic lithium, with a prominent feature near 55 eV (ref. [37]). The Li K-edge EELS spectra also reveal information about the inorganic species present in these samples, as the 'EtOH' sample appears to be dominated by LiF, while the 'no HA' sample has features of both LiF and LiOH in the SEI region[37].

## Revealing mechanisms of SEI disruption

Our cryo-EM results clearly demonstrate that adding ethanol disrupts the formation of a passivating SEI, leading to a disordered interfacial morphology quite different from the conventional picture of a clean Li–SEI interface that has dominated discourse in literature so far[21,29]. Moreover, from HRTEM, it appears that ethanol primarily changes the amorphous, organic components in the SEI, leaving inorganic, crystalline components intact. The disruption of amorphous SEI by ethanol is essential to nitrogen fixation via LiMEAS and could occur in a number of ways. One possibility is a *physical attack* on the SEI by the hydrogen bubbles that form when ethanol reacts with lithium, which could damage the mechanical stability of the SEI. Another possible mechanism is that the reaction between ethanol and lithium directly forms *favourable SEI species* that are poorly passivating and permeable to dinitrogen. Finally, it is also possible that ethanol *chemically attacks* the SEI, reacting with existing SEI materials to generate a more permeable interphase.

To determine which of these could be operative in our system, we employed XPS to study SEI chemistry with and without proton donor. Here we focus on the nitrogen-containing model systems (systems B and D), though spectra for all systems are included in Supplementary Figs. 27 and 28. Elemental analysis shows that with the addition of proton donor, the oxygen to carbon ratio in surface species increases while the fluorine to oxygen ratio decreases, implying that ethanol (two carbon atoms to one oxygen atom) may outcompete THF (four carbons to one oxygen) in SEI-forming reactions, while $BF_4^-$ breakdown may stay roughly the same. (Fig. 4a).

High-resolution spectra reveal this phenomenon in further detail (Fig. 4b). In the sample without ethanol, the prominent C 1*s* C–C (284.8 eV) and C–O (286 eV) signals and the O 1*s* C–O (533 eV) peak reveal organic SEI components consistent with THF decomposition products previously documented in literature, such as alkoxides (primarily lithium butoxide) and polymeric materials (such as PTMEG)[38–40]. With the addition of ethanol, the C 1*s* C–C peak decreases while the C–O signal grows, indicating organic species with shorter carbon chains and more oxygen, probably derived from ethanol rather than THF. The O 1*s* C–O signal intensity increases in samples with ethanol, widening to encompass binding energies typically associated with C=O (532 eV) and lithium alkoxide (ROLi, 530.3 eV) functionalities, indicating a greater diversity in oxygen-containing surface materials[41].

https://doi.org/10.1038/s41560-022-01177-5

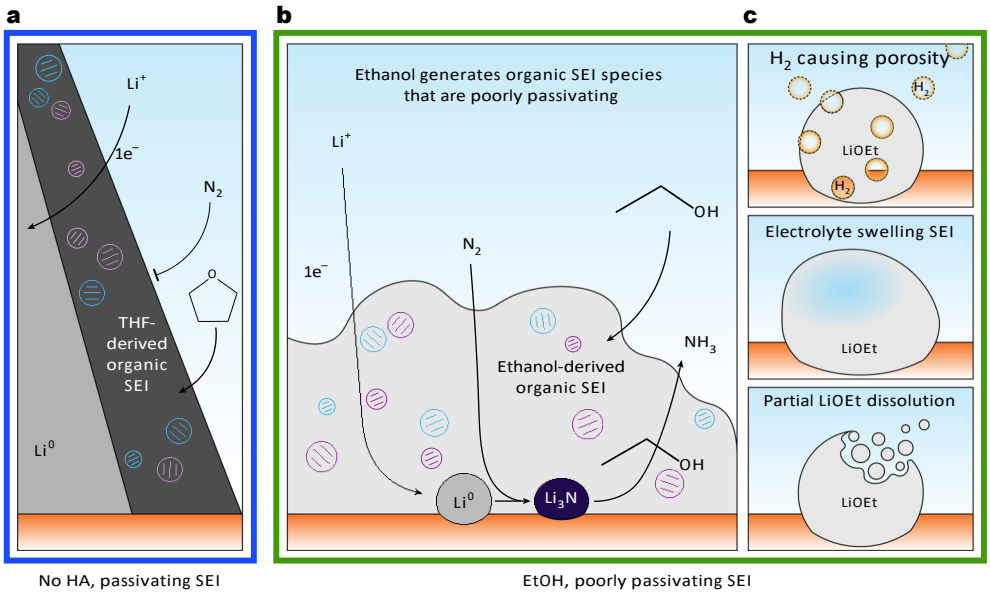


**Fig. 5 | SEI materials and their role in LiMEAS. a**, SEI generated by THF and $LiBF_4$ breakdown in the absence of proton donor inhibits $N_2$ reactivity with lithium. **b**, The addition of ethanol leads to organic components of the SEI that are permeable to nitrogen and other electrolyte components, enabling lithium reactivity including nitrogen fixation. **c**, Mechanisms by which ethanol-derived SEI materials could result in poor passivation. Top to bottom, poor passivation could result from hydrogen gas generation that induces porosity in the SEI, from a high degree of SEI swelling in electrolyte, or because of partial solubility of SEI components, such as lithium ethoxide (LiOEt).

XPS also offers insights into the composition of inorganic SEI components. In the F 1*s* spectra, both samples with and without ethanol show signals from LiF at 685 eV and a peak that can be attributed to other $Li_xBF_y$ species at higher binding energies that originate from the reduction of $LiBF_4$ on lithium[42]:

$$Li^0 + LiBF_4 \rightarrow LiF + Li_xBF_y \quad (1)$$

Both samples with and without ethanol show O 1*s* signal near the LiOH binding energy (531.7 eV) but no peak near that of $Li_2O$ (528 eV) (ref. [43]). This implies that the crystalline regions of the SEI with lattice spacing near 2.7–2.8 Å observed via HRTEM are more likely to be LiOH than $Li_2O$.

## Proton donor as a driver of surface reactivity

From these data, it appears that proton donor is the driver of surface phenomena in LiMEAS. In the absence of proton donor, the SEI is passivating, comprised of the breakdown products of $BF_4^-$ and THF. Nitrogen and electrolyte cannot permeate the SEI to react with lithium, but lithium ions can diffuse through, leading to accumulation of dendritic lithium (Fig. 5a). However, with the introduction of ethanol, the amorphous SEI species are dominated by ethanol breakdown products. Electrolyte and nitrogen can permeate this interphase, continuously consuming lithium as it deposits (Fig. 5b).

It is likely that a combination of the pathways identified above contribute to activation of the lithium surface for reaction with nitrogen. From product quantification, it is clear that ethanol reacts to form hydrogen gas, and gas generation has been shown to be associated with porous SEIs with poor mechanical stability (Fig. 5c)[44,45]. Additionally, the generation of hydrogen gas from the reaction of lithium with ethanol coproduces lithium ethoxide:

$$2Li + 2EtOH \rightarrow H_2 + 2LiOEt \quad (2)$$

Previous work proposes that lithium ethoxide could dissolve back into the electrolyte to serve as a shuttle for protons[14], but from XPS results, it is clear that some amount of ethoxide remains in solid form at the working electrode surface, participating in SEI formation. This ethoxide-rich SEI could itself be more 'permeable' to nitrogen. A cryo-EM study of vitrified interfaces demonstrates that SEIs swell in the presence of electrolyte, and that swelling increases in SEIs with a higher proportion of organic phases, which correlates with poor electrochemical cycling (and thus poor lithium passivation)[32]. Correspondingly, an ethanol-derived SEI may swell more in the presence of electrolyte, bringing dissolved nitrogen in closer contact with lithium and promoting continuous reactivity (Fig. 5c). Further, if lithium ethoxide is somewhat soluble in the electrolyte (Supplementary Fig. 28), the ethanol-derived SEI could lose material to dissolution (Fig. 5c).

Reactivity between ethanol or ethanol derivatives *with* the SEI is also possible. Previous work in our group has shown that even if the plating of lithium and presence of proton donor and nitrogen are separated temporally, ammonia is generated[29]. This implies that ethanol can attack a pre-existing, electrochemically formed SEI to facilitate lithium–nitrogen reactivity. Further discussion of possible modes of ethanol attack on the SEI can be found in Supplementary Note 10.

## Implications on LiMEAS mechanism

This study indicates that the materials previously proposed to act as electrocatalysts for LiMEAS[23] are not abundant on the working electrode surface. Stripping experiments performed in this electrolyte in the presence of nitrogen and ethanol detect no electrochemically connected lithium, making it unlikely that lithium acts as an electrocatalyst. Similarly, titration measurements reveal only ~0.3% FE going towards $Li_3N$, none of which was near enough to the surface for detection by XPS (Supplementary Methods). The other proposed electrocatalyst in LiMEAS is lithium hydride. Though most of the techniques used herein are not capable of detecting LiH, it reacts with protic molecules to form hydrogen gas[46,47] and thus is unlikely to be stable in the presence of ethanol. Rather, it appears that lithium and $Li_xN_yH_z$ species act as reactive intermediates; lithium nitridation and protonation are probably among several thermochemical pathways that consume lithium in this process, reactions that in the battery literature would be called 'chemical corrosion'[48].

## Towards design principles for LiMEAS SEIs

A major implication of these findings is that SEIs for LiMEAS must be poorly passivating to generate ammonia, but excessive reactivity between lithium and the proton donor can result in waste hydrogen gas and irreversible loss of active lithium to insoluble products. On the basis of this insight, it may be desirable to decouple the roles of SEI activation from protonation by first selecting a solvent/lithium salt combination for poor passivation of lithium, then choosing a proton donor with high stability. This approach could be combined with documented approaches such as the use of gas diffusion electrodes[17] and elevated $N_2$ pressures[18,19] to shift reactivity towards lithium nitridation rather than parasitic reactions with electrolyte. In this way, connecting SEI-forming reactions at the nanoscale to device-scale performance can guide the optimization of surface reactivity in LiMEAS.

## Conclusions

In this work, we took a multiscale approach combining product quantification with advanced imaging and characterization techniques to interrogate the role of surface chemistry in LiMEAS. The proton donor emerged as the key determinant of surface phenomena. In the absence of proton donor, the working electrode surface accumulates lithium in the form of mossy deposits with a passivating SEI that prevents lithium nitridation. With proton donor, metallic lithium reacts continuously with electrolyte and nitrogen, leaving behind a mosaic-structured SEI-like material with amorphous phases dominated by ethanol breakdown products. Together, these results revise our understanding of surface phenomena in LiMEAS and demonstrate that the lithium SEI can be a reactive interphase. Rather than a passivating SEI preserving the productivity of a metallic lithium deposit, the SEI in LiMEAS must allow lithium to react in a series of thermochemical reactions.

## Methods

### Preparation of electrolyte solutions

For experiments performed outside of the glovebox, THF (Acros Organics, ≥99%, stabilized with butylated hydroxytoluene) was dried over sieves before use. Molecular sieves (3 Å, 4–8 mesh, Acros Organics) were washed with acetone and dried in a furnace at 300 °C for 5 hours, then cooled to room temperature in an airtight container. Sieves were then added to a 500 ml round-bottom flask (approximately 25% v/v), and the flask was filled the rest of the way with THF and capped with a rubber stopper. The flask was kept covered in aluminium foil to avoid exposure to light. THF was allowed to dry undisturbed for at least 48 hours before use, and dry THF was used within 1–2 months of drying.

For experiments performed outside of the glovebox, $LiBF_4$ (Sigma-Aldrich, ≥99%) was weighed out in an argon glovebox then transferred out of the glovebox, where dry THF was added to obtain a 1 M solution of $LiBF_4$. The solution was centrifuged for 10 minutes at 1,610 × g to remove undissolved residue (possible contaminants), then the clear solution was transferred to oven-dried glass vials. Ethanol (VWR International, anhydrous, 200 proof, stored over sieves) was added to electrolyte requiring proton donor to make solutions of 0.1 M EtOH. Sealed electrolyte vials were stored in a desiccator and used on the day they were prepared.

For experiments performed in the glovebox, electrolyte was prepared in the glovebox. Any time solvents were used in the glovebox, the blowers of an activated carbon solvent trap (VAC Atmospheres) were turned on to increase circulation and capture excess solvent vapours. $LiBF_4$ was massed then dissolved in anhydrous THF (Sigma-Aldrich, ≥99.9%, stabilized with butylated hydroxytoluene) to make 1 M $LiBF_4$ solution. The solution was capped and sealed with parafilm, then removed from the glovebox to centrifuge for 10 minutes. After centrifuging, electrolyte was returned to the glovebox without opening the centrifuge tube, then distributed into oven-dried glass vials for storage. Ethanol (purged with argon and stored over sieves in the glovebox) was added to electrolytes requiring proton donor for a total concentration of 0.1 M. These electrolytes were also used on the day they were prepared.

### Working electrode preparation

Copper foil (Strem Chemicals, 99.9%) was used as the working electrode in all experiments, with new foils polished on the day of each experiment. Foils were cut to approximately 15 × 15 mm squares, rinsed with deionized water and then polished with 400 grit sandpaper followed by 1,500 grit sandpaper, using more deionized water to re-wet the surface and rinse the foils between sandpapers. Following polishing, foils were thoroughly rinsed with deionized water and dried in an 80 °C oven for at least 20 minutes before use.

### Daramic separator preparation

Ammonia yields were worse when using new Daramic separators, so a procedure was developed to 'break in' new separators. Daramic was soaked in THF for 12–24 hr, then rinsed with water. The THF used for soaking turned yellow in that time. Next, the separators were each used in an electrochemical cell using the usual LiMEAS set-up, with −3 mA chronopotentiometry run for 40 minutes. Separators were replaced when they became visibly cracked or when they became clogged (leading to higher resistances).

### Cell construction

All experiments were performed in two-compartment sandwich cells made of polyether ether ketone (PEEK) (Supplementary Fig. 1a). Copper foil was used as the working electrode, and platinum foil (Beantown Chemical, 99.99%) served as the counter electrode. Cells were designed such that the exposed electrode surface area is 1 $cm^2$. Daramic 175 was used as a separator, and aluminium foil current collectors were placed behind the counter and working electrodes to provide points of connection for the potentiostat leads. Unused holes in cell parts were sealed with ethylene tetrafluoroethylene (ETFE) Idex plugs. All cell parts were rinsed with deionized water and dried for at least 20 minutes before use, and all parts except for the copper working electrodes were reused for multiple experiments. Feed gas (argon or nitrogen) was flowed at 10 standard cubic centimeters per minute (sccm) using an Alicat gas flow controller. The gas was bubbled through dry tetrahydrofuran to saturate the stream and minimize electrolyte evaporation before being flowed into the bottom of the cell (Supplementary Fig. 2a,b). An electrolyte amount of 1.76 ml was added to each cell compartment before experiments.

### Ammonia, lithium nitride and hydrogen quantification experiments

Ammonia, lithium nitride and hydrogen were measured in parallel using this procedure, which was performed outside of the glovebox. Cells were constructed as described above, taking extra care to seal the cell parts together tightly. A 16-gauge needle was used to poke a hole in the Daramic separator at the top, above the fill line of the electrolyte, to equalize pressure between cell compartments. The counter electrode compartment was sealed with a plug, and the working electrode compartment was connected to a fluorinated ethylene propylene (FEP) tubing outlet that led to a water bubbler (to trap excess solvent), then to the gas chromatograph (GC). To ensure that gas did not escape from the cell, the pressure drop registered by the flow controller to flow 10 sccm gas through the GC inlet was noted before experiments, then experiments proceeded only if the flow controller pressure measurement exceeded this value once the whole cell set-up was constructed.

Each experiment started with 10 minutes at open circuit, then chronopotentiometry was performed at −3 mA for 20 minutes, passing 1 mAh 3.6 $C^{-1}$ in total. A model 8610 C SRI MultiGas 5 gas chromatograph was used for hydrogen quantification, with nitrogen as the carrier gas. Samples were injected through a 1 ml sample loop to a molecular sieve column held at 40 °C. A thermal conductivity detector was used to

quantify hydrogen, and separate calibrations were performed for argon and nitrogen experiments (Supplementary Fig. 5). The GC sampling sequence lasted 5 minutes and was run on repeat throughout open circuit voltage (OCV) and chronopotentiometry steps, and twice after the experiment ended to allow the gas from the cell time to reach the detector for a total of eight times. Hydrogen FEs were calculated by averaging the fourth through seventh hydrogen concentration points (Supplementary Fig. 4).

After the experiment, the GC line was disconnected from the cell. The electrolyte was removed, with the contents of the working electrode compartment saved for ammonia quantification using the salicylate method (below). The working electrode compartment was rinsed with ~1.76 ml of dry THF, then 1.76 ml of 0.1 M hydrochloric acid was added to protonate any residual fixed nitrogen species (for example, lithium nitride). The acid was allowed to sit in the cell compartment for about 60 s, then removed and added to 0.5 ml of 0.4 M sodium hydroxide to neutralize. The resulting sample was quantified using the salicylate method.

### Ammonia quantification via salicylate assay

The salicylate assay was used to quantify ammonia, following a procedure that has been described in previous work[14,17] and is elaborated on in the Supplementary Methods. In brief, two solutions were prepared: 2.5 M sodium salicylate plus 0.5 mM sodium nitroprusside ('salicylate solution') and a mixture of 10–15% NaOCl and 0.4 M NaOH in a 1:9 volume ratio ('hypochlorite solution'). Samples for ammonia and lithium nitride quantification were prepared at several different dilutions with a volume of 2 ml. The dilutions were prepared immediately following each experiment and could be stored sealed in a room-temperature drawer for up to three days before ammonia quantification. Typical dilutions for ammonia quantification were 10× (200 µl electrolyte + 1,800 µL DI water), 20× (100 µl electrolyte + 1,900 µl DI water) and 40× (50 µl electrolyte + 1,950 µL DI water). Typical dilutions for lithium nitride quantification were 2× (1 ml quantification solution + 1 ml DI water), 4× (0.5 ml quantification solution + 1.5 ml DI water) and 8× (0.25 ml quantification solution + 1.75 ml DI water). To these samples, 280 µl of salicylate solution, then 280 µl of hypochlorite solution were added in quick succession, then the samples were stored in darkness for at least 90 minutes to react, with the ammonia-containing samples turning blue in colour. Absorbance spectra were measured using a spectrophotometer, with the relevant quantity for calculating ammonia concentration taken to be the difference between absorbance at 650 nm and 475 nm (Supplementary Fig. 3a).

The relationship between absorbance and ammonia concentration was found using calibration solutions with known amounts of $NH_4Cl$, with a fresh calibration curve prepared each time quantification was performed (Supplementary Fig. 3b). Separate calibration curves were used for different dilutions of electrolyte and aqueous samples, usually 10×, 20× and 40× dilutions of electrolyte, plus an aqueous calibration curve for lithium nitride samples. Each calibration curve consisted of at least three concentration points, usually 0 µM, 30 µM and 60 µM. They were prepared by first adding the appropriate amount of DI water for a given dilution (1.80 ml, 1.90 ml, 1.95 ml or 2.00 ml for the 10×, 20×, 40× and aqueous dilutions, respectively), minus the appropriate amount of 1 mM $NH_4Cl$ solution to reach the desired concentration (0 µl, 60 µl or 120 µl for 0 µM, 30 µM and 60 µM samples, respectively). Then the $NH_4Cl$ solution was added, followed by the appropriate amount of unused electrolyte for the given dilution (200 µl, 100 µl, 50 µl or 0 µl for 10×, 20×, 40× and aqueous dilutions, respectively). The electrolyte used in calibration solutions was preferably less than a week old and stored in a desiccator, as older electrolyte could become cloudy with aging.

The FE of ammonia can be calculated from the concentration as follows:

$$FE_{NH_3} = \frac{C_{NH_3} V}{It/nF} \quad (3)$$

where $C_{NH_3}$ is the concentration of ammonia remaining in the electrolyte in moles per litre, $V$ is the volume of electrolyte removed from the catholyte compartment ($1.76 \times 10^{-3}$ l), $I$ is the current (0.003 A), $t$ is the total experiment time (1,200 s), $n$ is the moles of electrons transferred per mole of ammonia generated (3, regardless of whether the pathway is direct electroreduction or a thermochemical process mediated by electrodeposited lithium) and $F$ is Faraday's constant (96,485 C $mol^{-1}$ $e^-$). The same expression can be used to calculate the lithium nitride FW, with $C_{NH_3}$ representing the concentration of ammonia detected in the titrant and $V$ representing the volume of the sample.

### Residual metallic lithium quantification experiments

Metallic lithium remaining on the working electrode surface after experiments was quantified using the galvanostatic stripping procedure described below, which was performed outside of the glovebox. Cells were constructed as specified above, but with a platinum wire serving as a pseudo-reference electrode (RE).

Remaining electrochemically connected lithium on the working electrode surface was quantified using the following steps:

1. 10 min at open circuit to allow the potential to stabilize
2. 20 min chronopotentiometry, −3 mA $cm^{-2}$ (cathodic current, LiMEAS step)
3. 5 s at open circuit to record $E^{Li/Li+}$
4. ≤20 min chronopotentiometry, 3 mA $cm^{-2}$ (anodic current, stripping step), stopping when potential reaches 0 V versus pseudo-RE
5. 1 min at open circuit
6. ≤20 min chronopotentiometry, −3 mA $cm^{-2}$ (cathodic current) to strip away lithium deposited on the platinum counter electrode during step 4.

Metallic lithium FE was calculated as follows, with the stripping time $t_{strip}$ defined as the time needed for the slope of electrode potential (E) with respect to time (t) $\frac{dE}{dt}$ to surpass 0.03 V $s^{-1}$ (Supplementary Methods):

$$FE_{Li_0} = \frac{t_{strip}}{t_{LiMEAS}} \quad (4)$$

Taking the ratio of stripping versus deposition times is equivalent to a ratio of charge here because both steps were performed at constant currents of equal magnitude (3 mA).

### Electrochemical experiments run in glovebox

Experiments to prepare samples for SEM, TEM and XPS were all performed in an Ar glovebox with water and oxygen concentrations typically near 0.011 ppm and 0.1 ppm, respectively. For these experiments, cells were constructed as described above but with the separator adjusted to allow pressure equalization between the head spaces of the working and counter electrode compartments. This could be done either by using the same separators as the GC experiments, each of which had a small hole poked in the top using a 16-gauge needle, or by positioning the separators with a few millimetres of space between the top of the cell compartment and the top of the separator. The cells were stored in the oven if there was extra time between constructing them and bringing them into the glovebox.

The glovebox was plumbed with a gas line that could be used to flow argon or nitrogen saturated with electrolyte through sealed cells during experiments (Supplementary Fig. 2a). When not in use, the inlet and outlet gas lines were stored with both ends connected to each other such that they formed a loop and did not expose the glovebox to the outside environment.

Gas lines were set up such that a tee valve could select whether argon or nitrogen was flowed. While setting up the cell, regardless of the experiment, argon flowed through the gas inlet to prevent

contamination of the glovebox atmosphere. Additionally, whenever the outlet gas line was not connected to a sealed cell, the valve connecting it to ventilation was shut. Upon adding electrolyte to the cell, the counter electrode compartment was sealed with an Idex plug and the working electrode compartment was connected to the outlet gas line to allow continuous flow of gas in and out of the cell without exposing the glovebox atmosphere to nitrogen or excessive solvent vapours.

All experiments started with 10 minutes of open circuit to stabilize the potential. Then, 20 minutes of −3 mA $cm^{-2}$ current was applied using a Tekpower TP3005T d.c. power supply. After current application, the gas flow was switched to argon (if not already argon), and the cell rested for about a minute while any residual nitrogen could be flushed out of the head space to avoid contaminating the argon glovebox with nitrogen. Then, the gas outlet was disconnected, the electrolyte removed and the cell taken apart to prepare samples for imaging or characterization.

### SEM sample preparation and imaging

After running a constant current experiment in the glovebox as described above, the copper foil working electrode was carefully removed from the cell and gently rinsed with a few drops of anhydrous THF. Scissors were used to cut a ~1 cm long slice out of the foil, which was affixed to an SEM sample holder using conductive tape. Samples were allowed to dry in the glovebox for at least 20 minutes, then transferred into the SEM antechamber using a Semilab remote-controlled air-free sample transfer shuttle. All SEM imaging was conducted using a Zeiss Merlin high-resolution SEM set to an accelerating voltage of 10.00 kV with a probe current of 130 pA.

### Cryo-TEM sample preparation and imaging

For cryo-TEM experiments, cells were constructed as described above, but with one to four TEM grids incorporated into the working electrode set-up as illustrated in Supplementary Figs. 2c–e and 19. This set-up ensured that the grids were electrically connected to the copper working electrode and exposed to electrolyte and thus could accumulate lithium and its passivation species just like the rest of the working electrode. After the experiment, the cell was deconstructed and the TEM grids were carefully rinsed with a few drops of anhydrous THF. Grids were placed on a piece of Kim wipe and allowed to dry for a few minutes, then each grid was sealed in an individual Teflon-sealed Eppendorf tube by tightly capping it and wrapping with parafilm. The Eppendorf tubes were then removed from the glovebox and quickly plunged in liquid nitrogen (LN2) to freeze. Because the pressure in the glovebox, and thus the Eppendorf tube, was greater than ambient pressure, the tubes were air tight during transfer. Bolt cutters were used to quickly break open the Eppendorf tube and expose the grid to cryogen, and tweezers were used to move the grids into a cryo-grid box for storage, all under LN2. For ease of storage and transport, polypropylene centrifuge tubes with strings attached were used to scoop up the grid boxes in LN2 and then transferred to a thermos, with the strings used to label and access individual grid boxes. Samples could be stored in the thermos under LN2 for several hours before imaging.

To conduct cryo-TEM, samples were affixed to a Gatan 626 cryo-transfer holder using a cryo-transfer station to ensure that the whole process occurred under LN2. The transfer holder's built-in shutter was kept closed over the sample while inserting the sample into the TEM column (~1 s), preventing contact between the sample and air. After sample insertion, the cryo-transfer holder maintains the grid temperature at −178 °C. All TEM imaging was performed using a FEI Titan 80–300 scanning transmission electron microscope operated at an accelerating voltage of 300 kV, an instrument in the UCLA's CNSI's Electron Imaging Center for Nanomachines. It is equipped with an extreme field-emission gun (X-FEG), Oxford X-MaxTEM 100 N TLE Windowless silicon drift detector (SDD) 100 $mm^2$ EDS, and a Gatan Ultrascan 2 K × 2 K charge-coupled device (CCD) camera.

Electron flux is less than 100 e $Å^{-2}$ $s^{-1}$ for low-magnification TEM images and less than 1,000 e $Å^{-2}$ $s^{-1}$ for high-resolution TEM images. The electron beam exposure time of each image is no more than 30 s, and the acquisition time is 0.4 s to 1 s.

### XPS sample preparation and characterization

After running a constant current experiment in the glovebox as described above, the cell was deconstructed. The copper foil working electrode was removed from the cell and rinsed with a few drops of anhydrous THF. Scissors were used to cut a ~0.5 × 0.5 cm square from the Cu foil for analysis in XPS. Samples were affixed to an XPS sample holder using non-conductive tape and allowed to dry in the glovebox for at least 20 minutes. Samples were transferred to the XPS using an air-free transfer vessel[49]. Spectra were collected using a Physical Electronics Versaprobe II X-ray Photoelectron Spectrometer.

Spectra were processed using CasaXPS software. Binding energies were calibrated to the C 1*s* C–C peak at 284.8 eV, and high-resolution spectra were deconvoluted using a Shirley-type background for Li 1*s*, a linear background for all regions except Li 1*s* and a Gaussian/Lorentzian product line shape with mixing ratios between 30:70 and 50:50 Gaussian:Lorentzian.

## Data availability

The data collected and analysed for this work are included in the paper and its Supplementary Information. Source data are provided with this paper.

## References


1. MacFarlane, D. R. et al. A roadmap to the ammonia economy. *Joule* **4**, 1186–1205 (2020).
2. Erisman, J. W., Sutton, M. A., Galloway, J., Klimont, Z. & Winiwarter, W. How a century of ammonia synthesis changed the world. *Nat. Geosci.* **1**, 636–639 (2008).
3. *World Fertilizer Trends and Outlook to 2022* (FAO, 2019).
4. Maxwell, G. R. *Synthetic Nitrogen Products* (Kluwer Academic Publishers, 2004).
5. Smith, C., Hill, A. K. & Torrente-Murciano, L. Current and future role of Haber–Bosch ammonia in a carbon-free energy landscape. *Energy Environ. Sci.* **13**, 331–344 (2020).
6. Appl, M. in *Ullmann's Encyclopedia of Industrial Chemistry* 139–225 (2011).
7. Chen, J. G. et al. Beyond fossil fuel-driven nitrogen transformations. *Science* **360**, eaar6611 (2018).
8. Soloveichik, G. Electrochemical synthesis of ammonia as a potential alternative to the Haber–Bosch process. *Nat. Catal.* **2**, 377–380 (2019).
9. Comer, B. M. et al. Prospects and challenges for solar fertilizers. *Joule* **3**, 1578–1605 (2019).
10. Schiffer, Z. J. & Manthiram, K. Electrification and decarbonization of the chemical industry. *Joule* **1**, 10–14 (2017).
11. Ludwig, T., Singh, A. R. & Nørskov, J. K. Subsurface nitrogen dissociation kinetics in lithium metal from metadynamics. *J. Phys. Chem. C.* **124**, 26368–26378 (2020).
12. Tsuneto, A., Kudo, A. & Sakata, T. Efficient electrochemical reduction of $N_2$ to $NH_3$ catalyzed by lithium. *Chem. Lett.* **22**, 851–854 (1993).
13. Tsuneto, A., Kudo, A. & Sakata, T. Lithium-mediated electrochemical reduction of high pressure $N_2$ to $NH_3$. *J. Electroanal. Chem.* **367**, 183–188 (1994).
14. Lazouski, N., Schiffer, Z. J., Williams, K. & Manthiram, K. Understanding continuous lithium-mediated electrochemical nitrogen reduction. *Joule* **3**, 1127–1139 (2019).
15. Andersen, S. Z. et al. A rigorous electrochemical ammonia synthesis protocol with quantitative isotope measurements. *Nature* **570**, 504–508 (2019).

16. Greenlee, L. F., Renner, J. N. & Foster, S. L. The use of controls for consistent and accurate measurements of electrocatalytic ammonia synthesis from dinitrogen. *ACS Catal.* **8**, 7820–7827 (2018).
17. Lazouski, N., Chung, M., Williams, K., Gala, M. L. & Manthiram, K. Non-aqueous gas diffusion electrodes for rapid ammonia synthesis from nitrogen and water-splitting-derived hydrogen. *Nat. Catal.* **3**, 463–469 (2020).
18. Suryanto, B. H. R. et al. Nitrogen reduction to ammonia at high efficiency and rates based on a phosphonium proton shuttle. *Science* **372**, 1187–1191 (2021).
19. Li, K. et al. Enhancement of lithium-mediated ammonia synthesis by addition of oxygen. *Science* **374**, 1593–1597 (2021).
20. Fichter, F., Girard, P. & Erlenmeyer, H. Elektrolytische bindung von komprimiertem stickstoff bei gewöhnlicher temperatur. *Helv. Chim. Acta* **13**, 1228–1236 (1930).
21. Andersen, S. Z. et al. Increasing stability, efficiency, and fundamental understanding of lithium-mediated electrochemical nitrogen reduction. *Energy Environ. Sci.* **13**, 4291–4300 (2020).
22. Cai, X. et al. Lithium-mediated electrochemical nitrogen reduction: mechanistic insights to enhance performance. *iScience* **24**, 1–17 (2021).
23. Schwalbe, J. A. et al. A combined theory–experiment analysis of the surface species in lithium-mediated $NH_3$ electrosynthesis. *ChemElectroChem* **7**, 1542–1549 (2020).
24. Peled, E. The electrochemical behavior of alkali and alkaline earth metals in nonaqueous battery systems—the solid electrolyte interphase model. *J. Electrochem. Soc.* **126**, 2047–2051 (1979).
25. Peled, E. & Menkin, S. Review—SEI: past, present and future. *J. Electrochem. Soc.* **164**, A1703–A1719 (2017).
26. Cheng, X. B. et al. A review of solid electrolyte interphases on lithium metal anode. *Adv. Sci.* **3**, 1500213 (2016).
27. Zachman, M. J., Tu, Z., Choudhury, S., Archer, L. A. & Kourkoutis, L. F. Cryo-STEM mapping of solid–liquid interfaces and dendrites in lithium-metal batteries. *Nature* **560**, 345–349 (2018).
28. Li, Y. et al. Correlating structure and function of battery interphases at atomic resolution using cryoelectron microscopy. *Joule* **2**, 2167–2177 (2018).
29. Lazouski, N. et al. Proton donors induce a differential transport effect for selectivity toward ammonia in lithium-mediated nitrogen reduction. *ACS Catal.* **12**, 5197–5208 (2022).
30. Cherepanov, P. V., Krebsz, M., Hodgetts, R. Y., Simonov, A. N. & MacFarlane, D. R. Understanding the factors determining the Faradaic efficiency and rate of the lithium redox-mediated $N_2$ reduction to ammonia. *J. Phys. Chem. C.* **125**, 11402–11410 (2021).
31. Li, Y. et al. Atomic structure of sensitive battery materials and interfaces revealed by cryo-electron microscopy. *Science* **358**, 506–510 (2017).
32. Zhang, Z. et al. Capturing the swelling of solid-electrolyte interphase in lithium metal batteries. *Science* **375**, 66–70 (2022).
33. Verdouw, H., Van Echteld, J. A. & Dekkers, E. M. L. Ammonia determination based on indophenol formation with sodium salicylate. *Water Res.* **12**, 399–402 (1977).
34. Adams, B. D. et al. Accurate determination of coulombic efficiency for lithium metal anodes and lithium metal batteries. *Adv. Energy Mater.* **8**, 1702097 (2018).
35. Xiao, J. et al. Understanding and applying Coulombic efficiency in lithium metal batteries. *Nat. Energy* **5**, 561–568 (2020).
36. Mehta, R. in *Scanning Electron Microscopy* (ed. Kazmiruk, V.) 17–30 (InTech, 2012).
37. Wang, F. et al. Chemical distribution and bonding of lithium in intercalated graphite: identification with optimized electron energy loss spectroscopy. *ACS Nano* **5**, 1190–1197 (2011).
38. Aurbach, D., Daroux, M. L., Faguy, P. W. & Yeager, E. Identification of surface films formed on lithium in dimethoxyethane and tetrahydrofuran solutions. *J. Electrochem. Soc.* **135**, 1863–1871 (1988).
39. Kanamura, K., Tamura, H., Shiraishi, S. & Takehara, Z. XPS analysis of lithium surfaces following immersion in various solvents containing $LiBF_4$. *J. Electrochem. Soc.* **142**, 340–347 (1995).
40. Zhuang, G. R., Wang, K., Chen, Y. & Ross, P. N. Study of the reactions of Li with tetrahydrofuran and propylene carbonate by photoemission spectroscopy. *J. Vac. Sci. Technol. A* **16**, 3041–3045 (1998).
41. Andersson, E. K. W. et al. Early-stage decomposition of solid polymer electrolytes in Li-metal batteries. *J. Mater. Chem. A* **9**, 22462–22471 (2021).
42. Parimalam, B. S. & Lucht, B. L. Reduction reactions of electrolyte salts for lithium ion batteries: $LiPF_6$, $LiBF_4$, LiDFOB, LiBOB, and LiTFSI. *J. Electrochem. Soc.* **165**, A251–A255 (2018).
43. Wood, K. N. & Teeter, G. XPS on Li-battery-related compounds: analysis of inorganic SEI phases and a methodology for charge correction. *ACS Appl. Energy Mater.* **1**, 4493–4504 (2018).
44. Li, Y. et al. Revealing nanoscale passivation and corrosion mechanisms of reactive battery materials in gas environments. *Nano Lett.* **17**, 5171–5178 (2017).
45. Han, B. et al. Poor stability of $Li_2CO_3$ in the solid electrolyte interphase of a lithium-metal anode revealed by cryo-electron microscopy. *Adv. Mater.* **33**, 2100404 (2021).
46. Smith, R. L. & Miser, J. W. *Compilation of the Properties of Lithium Hydride* (NASA, 1963).
47. Aurbach, D. & Weissman, I. On the possibility of LiH formation on Li surfaces in wet electrolyte solutions. *Electrochem. Commun.* **1**, 324–331 (1999).
48. Boyle, D. T. et al. Corrosion of lithium metal anodes during calendar ageing and its microscopic origins. *Nat. Energy* **6**, 487–494 (2021).
49. Stevie, F. A., Garcia, R., Shallenberger, J., Newman, J. G. & Donley, C. L. Sample handling, preparation and mounting for XPS and other surface analytical techniques. *J. Vac. Sci. Technol. A* **38**, 063202 (2020).

## Acknowledgements

K.M., K.S. N.L., and C.K.K. gratefully acknowledge support by the National Science Foundation under grant number 2204756. K.S. and N.L. acknowledge support from the National Science Foundation Graduate Research Fellowship under grant number 1745302. Cryo-EM data were acquired at the Electron Imaging Center for Nanomachines (EICN) at the University of California, Los Angeles's California NanoSystems Institute (CNSI). Y.L. and X.Y. were supported in part by the National Science Foundation under grant number CBET-2143677. This work also made use of the MRSEC Shared Experimental Facilities at Massachusetts Institute of Technology (MIT), supported by the National Science Foundation under award number DMR-1419807. We thank the staff scientists at both UCLA EICN and MIT MRSEC for their training and expertise. We also thank M. Wolski of Daramic for providing us with polyporous separator samples, F. Frankel for feedback on figure design and K. Williams, N. Corbin, H. J. Song, G. Junor, G. Hobold and all the members of the Li and Manthiram research groups for productive and helpful discussions.

## Author contributions

K.S., K.M. and Y.L. conceptualized the paper. K.S. developed the experimental methodology for product quantification, sample preparation for imaging and characterization and collection of XPS spectra. X.Y. and Y.L. developed the experimental methodology for SEM and cryo-EM. K.S. performed product quantification, SEM imaging and XPS experiments, and K.S. and C.K. prepared

samples for cryo-EM. X.Y. carried out cryo-EM and SEM imaging. Y.L. performed EELS characterization. M.M. advised on microscopy and imaging analysis. C.K. and K.S. performed the validation. K.S. prepared the figures and wrote the original draft of the manuscript and Supplementary Information, and N.L, Y.L., K.M., C.K., X.Y. and K.S. reviewed and edited its contents. K.M. and Y.L. supervised the work.

## Competing interests

The authors declare no competing interests.

## Additional information

**Supplementary information** The online version contains supplementary material available at https://doi.org/10.1038/s41560-022-01177-5.

**Correspondence and requests for materials** should be addressed to Karthish Manthiram or Yuzhang Li.

**Peer review information** *Nature Energy* thanks Matteo Cargnello, Chongmin Wang and the other, anonymous, reviewer(s) for their contribution to the peer review of this work.